Libraries and Learning Services

University of Auckland Research Repository, ResearchSpace

Version

This is the Accepted Manuscript version. This version is defined in the NISO recommended practice RP-8-2008 http://www.niso.org/publications/rp/

Suggested Reference

Copyright

Accepted Manuscript

Effects of interfacial heat transfer, surface tension and contact angle on the formation of plasma-sprayed droplets through simulation study

Yongang Zhang, Steven Matthews, A.T.T. Tran, Margaret Hyland

Please cite this article as: Yongang Zhang, Steven Matthews, A.T.T. Tran, Margaret Hyland, Effects of interfacial heat transfer, surface tension and contact angle on the formation of plasma-sprayed droplets through simulation study, *Surface & Coatings Technology* (2016), doi:10.1016/j.surfcoat.2016.09.066

Effects of interfacial heat transfer, surface tension and contact angle on the formation of plasma-sprayed droplets through simulation study

Yongang Zhang[*] yzha711@aucklanduni.ac.nz; Steven Matthews; A.T.T. Tran; Margaret Hyland

Department of Chemical and Materials Engineering, the University of Auckland, 314-390 Khyber Pass Road, Auckland

[*]Corresponding author.

A full length of the abstract.

A comprehensive numerical study of the effects of interfacial heat transfer, surface tension (1.8 n/m, 1.647 n/m, 1.35 n/m and temperature-dependent values) and contact angles (60°, 90° and 120°) on the droplet spreading behaviour in the formation of the plasma-sprayed splats was conducted. The evolution of splat morphologies with time was accurately captured using a volume of fluid (VOF) model in a 2-D computational domain. The results show that bubbles form at the time of impact and decrease the heat transfer efficiency at the contact points. During spreading, solidification occurs at the droplet edge before maximum spreading. The rapid growth of the underlying solidified layer induces fluid instabilities for the upper liquid layer, which triggers material jetting. The interfacial heat transfer is the key parameter influencing the droplet cooling process and the final splat morphology. Increasing the substrate preheating temperatures (from 27°C to 300°C) delays solidification but increases the potential of substrate melting. A low surface tension (1.35 n/m) readily promotes liquid projections, while the contact angle is of less importance in changing the surface morphologies.

Keywords: droplet spreading, cross-sectional splat morphologies, plasma spraying, numerical simulation

Nomenclature			
General symbols		*Greek symbols*	
D_0	Droplet diameter before impact	α	volume fraction of fluid
V_0	droplet velocity before impact	ρ	density
t	time	μ	viscosity
v	velocity	σ	surface tension
g	gravitational acceleration	β	liquid fraction
k	thermal conductivity	ξ_m	maximum flattening ratio
P	pressure	θ	liquid-solid contact angle
T	temperature	κ	surface curvature
D	droplet spreading diameter		
H	total enthalpy	*Dimensionless numbers*	
h	sensible enthalpy	Co	Courant number($= vdt/dx$)
ΔH	latent heat	We	Weber number ($= \rho V_0^2 D_0 / \sigma$)
S	solidification parameter	Re	Reynolds number ($= \rho V_0 D_0 / \mu$)

L	latent heat of the liquid phase	s^*	thickness of solidified layer $(= s / D_0)$
x, y, z	coordinate	Ma	Marangoni number $(= \rho C_p D |d\sigma / dT| \Delta T / 2\mu k)$
s	thickness of the solidified layer		
n	the surface normal at the interface		
C_p	specific heat	*Subscript symbols*	
A_{mush}	mushy zone constant	l	liquid
S_m	source term	g	gas
F_{vol}	volume surface tension force	w	wall

1 Introduction

During plasma spraying, powder particles are injected into the plasma stream, where they experience melting and acceleration. The molten (or semi-molten) droplets impact on the substrate surface, spread and solidify to form splats with different morphologies. The splats served as the basic block of the bulk coating. Such droplet impingement onto the substrate with small diameter scales, high temperatures and velocities involves complex phenomena such as fluid dynamics, solidification, bubble entrapment and interfacial heat transfer. Because all these characteristics occur in the magnitude of microseconds, it is impossible to clearly reveal the entire impact and spreading process in the formation of splats through experimental methods [1, 2]. Therefore, computational fluid dynamics (CFD) simulation provides a good alternative to study droplet impact dynamics. The explicit volume of fluid (VOF) model with small time steps is used to accurately capture the transient liquid-gas interface. This model has been widely used in understanding the impact and spreading characteristics of liquid droplets in the range of micrometre- and millimetre-sized water and tin droplets [3-6] and plasma sprayed micrometre metal/oxide droplets [7-10]. The impact dynamics of millimetre-sized isopropanol with low impact velocities onto the preheated substrates were numerically studied [3]. The predicted droplet spreading morphologies and interfacial temperatures demonstrated a good agreement with experimental observation. Tabbara et al. [4] simulated the spreading behaviour of a 2.2 mm molten tin particle at different impacting velocities based on the VOF and solidification models. The growth of the solidified layer experienced three stages of planar morphology, uneven morphology and wave mixing. Through solving a fixed-grid Eulerian model, the spreading behaviour of the molten droplets, either in the micrometre size [7] or millimetre size [5], with interfacial heat transfer and solidification, were successfully simulated using 3-D models. Zheng et al. [8] also used the commercial software ANSYS FLUENT to describe the evolution of contact pressure, velocity and temperature fields and solidification in the formation of plasma-sprayed zirconia splats. With ANSYS CFX software, Tran et al. [9] predicted substrate melting and resolidification when molten Ni droplets flattened on stainless steel, and validated the model with experimental observation. Apart from the VOF method, Oukach et al. [11] modelled the spreading behaviour of molten alumina droplets using the Level Set method to track liquid-gas interface.

The formation of single splats in plasma spraying is dependent on a range of factors, such as the high temperature thermal-physical properties of the powder material, the substrate temperature, the droplet contact angle on the substrate surface and the thermal contact resistance along the splat-substrate interface. Through mathematical modelling, Wan et al. [12] found that the surface tension and contact angle were negligible in changing splat spreading diameters during plasma spraying. The substrate preheating conditions and interfacial thermal contact resistance were found to be the key factors influencing droplet spreading diameters, by means of influencing the solidification process. Unfortunately, the instantaneous splat morphology and solidification process were not demonstrated in detail. A clear display is important for understanding how the solidification behaviour influences liquid flowability. Nevertheless, the contact angles were found to be dominant in determining the spreading dynamics without considering the solidification process especially in the case of millimetre-sized liquid droplet [13, 14]. More work should be conducted on understanding the role of contact angles on droplet spreading when taking into account of the solidification.

Many research groups have focused on studying the splat formation of nickel powder [2, 7]. Therefore, nickel material was selected in the simulation for consistently studying droplet spreading behaviour, which may give more informative understanding. Moreover, chromium served as the active element and found to improve static wetting behaviour of droplets [15]. Our previous experimental study showed that droplet fragmentation was supressed for Ni20Cr splats compared to Ni splats, and more disk shapes were observed for Ni20Cr material [16]. It has been found that one of the main differences between the high temperature thermophysical properties for Ni and Ni20Cr was the liquid surface tension, which was correlated with the droplet contact angles and wettability. However it is still unclear whether the formation of more Ni20Cr disk splats results from the difference in surface tension values, or other effects such as interfacial reactions and dynamic wetting with the addition of Cr element. Therefore it is important to verify the role of contact angle, surface tension and interfacial heat transfer on droplet spreading dynamics in plasma-sprayed splat formation.

In this paper, the behaviour of droplet impact, spreading and solidification was comprehensively studied through CFD simulation. Through accurately demonstrating the time-dependent spreading process and solidification behaviour by simulation, the influence of interfacial heat transfer (consisting of substrate preheating and interfacial thermal contact resistance (TCR)), droplet surface tension and contact angles on droplet spreading were investigated. It should be noted that in this paper the scope is constrained to understanding the droplet impact onto the substrate where there was no surface adsorbents/moisture evaporation. Splat fragmentation induced by the evaporation of surface adsorbents/moisture was not studied numerically.

2 Numerical models

2.1 Computational domain and meshing

The commercial software ANSYS FLUENT 16.0 [17] was used to model the droplet impact and spreading dynamics. A molten Ni droplet of 54 μm diameter with an initial temperature of 2100 K was simulated to impact onto a stainless steel substrate with an initial velocity of 100 m/s. The high temperature thermophysical properties of the Ni droplet and the stainless steel substrate are summarized in Table 1. Three different values of surface tension were used in this paper for understanding its effect on droplet spreading. The value of 1.8 n/m represents the Ni surface tension at melting point (1728K), while the value of 1.647 n/m represents the Ni surface tension at initial impact temperature (2100K). The value of 1.35 n/m represents a surface tension comparable with Ni20Cr material at its melting point (more information can be found in Section 3.3). A two dimensional (2D) axisymmetric domain was used in the simulation where the size of air domain was 320 μm x 90 μm, large enough to decrease the backward flow to the boundaries. The dimension of the substrate domain was 320 μm x 25 μm (width X and height Y). Detailed boundary conditions are presented in Fig. 1. When the liquid droplet flowed over the substrate surface, a non-slip wall boundary condition was utilized. This condition assumed that there was no relative velocity between the fluid and stationary substrate surface at the contact line. In reality the contact line would experience slip during droplet spreading. So the definition of a slip length was proposed, considering the velocity gradient at the triple line, to avoid the singularity [18]. Nevertheless, this length scale was much smaller than the grid spacing in the numerical studies [19, 20]. Thus the simplest assumption of a non-slip wall condition was acceptable to predict droplet spreading behaviour. Because of the difficulties in photographing the droplet spreading process, the dynamic contact angles (DCA) cannot be measured along the contact line. Therefore the equilibrium static contact angle (SCA) was used in the present paper [5]. Qualitatively, the predictions of droplet spreading ratios of DCA and SCA were in a good agreement [6, 21].

Table 1 Thermophysical properties of the Ni droplet and stainless steel substrate in simulation [22, 23].

Material	Melting point K	Density kg/m^3	Thermal conductivity W/m·K	Specific heat J/kg·K	Latent heat J/kg	Viscosity Pa·s	Surface tension N/m
Ni	1728	7850 (l) 8450 (s)	69.2 (l) 80 (s)	735 (l) 595 (s)	2.92x10^5	0.006	1.35 1.647 1.8
Stainless steel	1723	7854	15	480			
							l: liquid and s: solid.

The meshing quadrilateral element numbers were fixed with 56,000 elements for the substrate domain and 705,600 elements for the air domain. The smallest grid in the air domain was 0.14 μm to accurately capture the droplet-air interface motion. An extensive grid independence test was conducted to confirm that the meshing scheme was sufficiently fine to capture the droplet spreading diameter and the droplet-air interface. In the testing study, three

different grid sizes were selected, yielding a minimum cell length of 0.2 µm (400,000 cells in total), 0.14 µm (761,600 cells) and 0.11 µm (1,238,400 cells). The meshing algorithm used in this paper (grid size 0.14 µm) was sufficiently fine to capture the interface, generating an estimated error around 1.5% for the characteristic spreading ratios as shown in Fig. 2. The grid independence tests were conducted under the condition of substrate preheating 300°C, thermal contact resistance $5x10^{-7}$ m^2K/W, contact angle 60° and temperature-dependent surface tension. For obtaining disk Ni splats on stainless steel substrates, the interfacial thermal contact resistance was found to be in the range of $1x10^{-7}$- $1x10^{-6}$ m^2K/W [7, 24, 25]. Therefore the thermal contact resistance was chosen from this range.

2.2 The VOF model

The VOF model is used to compute the volume fraction of fluid (α_1) and gas (α_g) to track the movement of the droplet-air interface. In each control volume, the parameter α is defined as unity in the cell fully occupied by the liquid droplet and zero in the cell fully occupied by the air. The value α between zero and unity points to the liquid-air interface and in every cell the volume fractions of these two phases sum to unity as expressed in Eq. 1. In this paper, the surrounding air was treated as the primary phase.

$$\alpha_1 + \alpha_g = 1 \quad (1)$$

Therefore the fields for all variables and properties are shared by the phases and represent volume-averaged values. The related material density and viscosity are expressed by Eq. 2 and 3.

$$\rho = \alpha_1\rho_1 + \alpha_g\rho_g \ (2)$$

$$\mu = \alpha_1\mu_1 + \alpha_g\mu_g \ (3)$$

where ρ_1 and ρ_g represent the density of the liquid droplet and air respectively while μ_1 and μ_g represent the viscosity of the liquid droplet and air respectively.

The location of the moving interface between the molten liquid and air is computed by solving volume fraction continuity equation for the liquid phase, as expressed in Eq. 4.

$$\frac{\partial \alpha_1}{\partial t} + \vec{v} \cdot \nabla \alpha_1 = 0 \ (4)$$

The axisymmetric governing equations of momentum (Eq. 5) and energy (Eq. 6) in the computational domain are expressed as follows.

$$\frac{\partial}{\partial t}(\rho \vec{v}) + \nabla \cdot (\rho \vec{v} \vec{v}) = -\nabla P + \nabla \cdot [\mu(\nabla \vec{v} + \nabla \vec{v}^T)] + \rho \vec{g} + \vec{F}_{\mathrm{vol}} + \vec{S}_{\mathrm{m}} \quad (5)$$

$$\frac{\partial(\rho H)}{\partial t} + \nabla \cdot (\rho \vec{v} H) = \nabla \cdot (k_{\mathrm{eff}} \nabla T) \quad (6)$$

For Eq. 5, $\rho \vec{g}$ is the gravitational body force, k_{eff} is the effective thermal conductivity ($k_{\mathrm{eff}} = \alpha_l k_l + \alpha_g k_g$), S_{m} is the source term induced by the solidification process as described in Eq. 13 (see section 2.3) and $\vec{F}_{\mathrm{vol}}$ is the volume surface tension force solved using the continuum surface tension (CSF) model of Brackbill et al. [26] as expressed in Eq. 7.

$$\vec{F}_{\mathrm{vol}} = \sigma \kappa \nabla \alpha_l \quad (7)$$

where σ is the droplet surface tension coefficient and κ is the surface curvature calculated from the local gradients in the surface normal at the interface, as expressed in Eq. 8.

$$\kappa = -(\nabla \cdot \vec{n}) = \frac{1}{|n|}[(\frac{n}{|n|} \cdot \nabla)|n| - (\nabla \cdot n)] \quad (8)$$

where $n = \nabla \alpha_l$ represents the surface normal at the interface.

Meanwhile, the VOF model can be augmented to include wall adhesion effects through the contact angle θ between the droplet and the substrate wall. The wall adhesion effects help to adjust the surface curvature near the wall, as expressed in Eq. 9.

$$\vec{n} = \vec{n}_{\mathrm{w}} \cos \theta + \vec{t}_{\mathrm{w}} \sin \theta \quad (9)$$

where $\vec{n}_{\mathrm{w}}$ and $\vec{t}_{\mathrm{w}}$ represent the unit vectors normal and tangential to the wall respectively.

In the calculations of volume fraction parameters, an explicit time scheme was used where the time step was controlled by the Courant number ($Co = v\frac{dt}{dx}$, v velocity, t time and x grid spacing). At the regime of high droplet impact and spreading velocity, a very small time step of 1×10^{-10}s was used to meet the requirement of Co number (less than 0.25). After 4 μs spreading, a larger time step 5×10^{-10} s was used to save computational time.

For Eq. 6, H is the total material enthalpy as described in the next section 2.3, k is the thermal conductivity and T is the temperature.

2.3 The solidification model

The FLUENT software uses a parameter of liquid fraction, β, to implicitly represent the melt interface based on the enthalpy-porosity method calculating the enthalpy balance. The total enthalpy of the material is calculated as the sum of the sensible enthalpy h and the latent heat ΔH, expressed in Eq. 10.

$H = h + \Delta H$ (10)

Where

$$h = h_{\text{ref}} + \int_{T_{\text{ref}}}^{T} C_p dT$$

where h_{ref} stands for the reference enthalpy at the reference temperature T_{ref} and the C_p is the specific heat.

The values β of zero and unity represent the solid and liquid in the control volume respectively, through determining whether the temperature reaches the solidus point. Values between zero and unity represented the solidification interface, also named the mushy zone.

$$\beta = \begin{cases} 0 & \text{if } T < T_{\text{solidus}} \\ 1 & \text{if } T > T_{\text{liquidus}} \\ (T - T_{\text{solidus}})/(T_{\text{liquidus}} - T_{\text{solidus}}) & \text{if } T_{\text{solidus}} < T < T_{\text{liquidus}} \end{cases} \quad (11)$$

As can be seen in the Eq. 11, the mushy zone consists of the solid and liquid phases. As the temperature decreases and induces solidification, the latent heat of the liquid dissipates. According to the liquid fraction existing inside the control cell, the dissipated latent heat can be expressed as Eq. 12.

$\Delta H = \beta L$ (12)

where L is the latent heat of the liquid material.

The enthalpy-porosity method calculates the effect of solidification on the whole velocity field by treating the mushy zone as a porous medium. Once the computational cell is fully occupied by the solid, the associated velocities become zero. Therefore a source term S_m, given by Eq. 13 is added to the velocity equation.

$$\vec{S}_m = \frac{(1-\beta)^2}{(\beta^2 + 0.001)} A_{\text{mush}} \vec{v} \quad (13)$$

where A_{mush} is the mushy zone constant and equals to 1×10^9 in this paper, suggested by [8].

2.4 Numerical method

All the governing equations are solved using the segregated pressure-based solver in FLUENT. The momentum and energy equations were discretised using the QUICK scheme. The pressure-velocity coupling was achieved through the PISO method during the transient calculation. The VOF equations were discretized through the geo-reconstruct approach which accurately tracked the liquid-gas interface motion. The gradients of variables in the governing equations were computed using the Green-Gauss Node based method to obtain a second-order spatial accuracy. The pressure values were interpolated using the PRESTO! approach in

the computational cells. In order to understand the heat transfer process during droplet impact, two monitor points were selected. One was located at the droplet top surface on the axis of symmetry and the other one was located at the centre of substrate surface.

3 Results and discussion

3.1 Splat morphology evolution

The evolution of droplet spreading behaviour and the solidification process on a substrate preheated at 300°C are shown in Fig. 3. The surface tension of the droplet was set to be 1.8 n/m with a contact angle of 90° and thermal contact resistance of 1×10^{-7} m^{2}K/W. All the following results were demonstrated under this condition if not specified. The Weber (We) and Reynolds (Re) numbers are 2355 and 7065 respectively, using the parameters at the initial impact moment. We and Re numbers are expressed as the following equations,

$$Re = \frac{\rho V_0 D_0}{\mu} \quad (14)$$

$$We = \frac{\rho V_0^2 D_0}{\sigma} \quad (15)$$

where ρ is droplet density, V_0 impact velocity and D_0 the original particle diameter.

At the very initial droplet impact stage (0.05 µs in Fig. 3a), a very short finger jetted out radially. Under the condition of capillary force, this short finger would potentially break up to form small secondary droplets (see 0.12 µs in Fig. 3b). Meanwhile, due to the high impact velocity, an air vortex was observed at the outside surface which would force more air to be entrapped inside the liquid droplet. Bubble formation was clearly observed at the centre line along the droplet-substrate interface. Upon droplet impact, high impacting pressures could drive gas supersaturation and bubble nucleation [27]. With time evolution to 0.5 µs, a thin solidified layer was formed at the periphery during droplet spreading because this part was thinner than the rest and thus contained less thermal energy to transfer. This also indicated that solidification occurred inside the droplet before reaching its maximum diameter. Then the solidification front gradually extended to the droplet surface at 1 µs. Once the solidification reached the top surface, a protuberant wedge was formed. This protuberance disturbed liquid flowability and induced instability. Therefore the streamlines were visibly lifted up, indicating a potential jetting of the edge liquid. Some jetted materials were clearly observed at 3.5 µs which implies that solidification influenced droplet spreading kinetics. Driven by the kinetic energy, more liquid material spread to the rim, leading to a thicker edge. However, the solidification was fully completed at the peripheral part while a small proportion of liquid was still present on the top surface at the centre. Solidification process was complete for the whole splat around 4 µs and assumed a disk shape with some ejected materials. Notably, the thickness of the underlying solidified layer was not uniform during droplet spreading. Numerous small bubbles were entrapped along the splat-substrate interface

and inside the solidified microstructure. This also validated that the meshing was fine enough to describe the fluid motion.

In order to validate the 2D simulation results, a 3D simulation was conducted for studying the spreading behaviour of a 50 μm Ni droplet under the same impact conditions. The calculation was carried out in the axisymmetric one fourth domain where the air and substrate domains had a dimension of 120 μm x 120 μm x 80 μm and 120 μm x 120 μm x 25 μm (length X, width Y and height Z) respectively. The total meshing contained 3,822,000 grids for accurately tracking the droplet-air interface. Fig. 4 gives the final splat morphologies of the top view and cross sections from the 3D simulations, which qualitatively agreed with the 2D results. Although the 3D simulation could give more details about the droplet spreading behaviour at different directions, the 2D simulation greatly saved computational effort in the investigation of the effects of thermal contact resistance, substrate preheating, surface tension and contact angles on droplet spreading behaviour. Therefore, 2D simulation reasonably revealed the overall splat morphology evolution and all the analyses in this paper were based on 2D modelling results. In addition, two typical splat morphologies of disk shapes (type 3 and type 4) for plasma-sprayed Ni powder are shown in Fig. 5. Our ability to reproduce disk splat shapes through 2D and 3D modelling gives confidence in the modelling results.

Two splat types of disk shape are shown in Fig. 5. Type 3 splats represented a disk shape with splashing fingers while type 4 represented perfect disk shapes. This definition was consistent with our previous experimental observation. Table 2 summarizes the statistic results of fractions and flattening ratios of type 3 and type 4 splats for Ni and Ni20Cr materials at substrate preheating temperature of 300°C. For each material, 100 splats were measured. A statistical method t-test was utilized to examine whether the flattening ratios were similar or not. Ni20Cr splats intended to generate splashing fingers, achieving a larger fraction of type 3 splats. However, larger spreading ratios were observed for Ni20Cr material regardless of splat shapes. This trend was also confirmed by t-test analysis where a value smaller than 0.05 statistically represents dissimilarities of the collected data.

Table 2 Fractions and flattening ratios of type 3 and type 4 splats for Ni and Ni20Cr materials

	Ni		Ni20Cr		t-test
	Fraction	Flattening ratio	Fraction	Flattening ratio	
Type 3	56%	4.71±0.80	62%	4.96±0.60	<0.05
Type 4	44%	4.70±0.64	38%	5.24±0.46	<0.05

3.2 Effect of interfacial heat transfer

Figure 6 depicts the influence of thermal contact resistance on droplet spreading behaviour on substrates preheated at 150°C. The spreading diameter was measured based on the contact area between the droplet and substrate, excluding the splashed fingers. At the maximum spreading diameter, the solidification process was almost complete at the outer edge. With increasing thermal contact resistance, a larger fraction of liquid was observed (see Fig. 6a) at the centre indicating that droplets remained in liquid form for a longer time. The large thermal contact resistance slowed down droplet solidification. Therefore more inertial energy

was expended in promoting droplet spreading, which generated thinner splats due to the large extent of spreading. In addition, more liquid material accumulated at the periphery. It is reasonable to predict that the droplet would become thin enough to rupture inside the droplet main body with a higher thermal contact resistance, as a result of overspreading. In a short period after impact, the flattening ratios quickly increased regardless of the different heat conduction rate because the inertial force dominated droplet spreading as shown in Fig. 6b. After maximum spreading, the droplet tended to recede slightly due to the surface tension. The experimentally measured flattening ratio for Ni splats [16] was also compared with the simulated results. The mean flattening ratio was comparable with the simulated results where the thermal contact resistance was 5×10^{-7} $m^2 K/W$. One should note that the wide variation of the experimentally measured ratios was probably due to the original powder distribution (45-63 µm).

Figure 7 shows the influence of the thermal contact resistance on droplet spreading behaviour at a higher preheating temperature of 300°C. As shown in Fig. 7a, similar spreading behaviour was found compared with that at the lower preheating temperature of 150°C. The small thermal contact resistance facilitated heat conduction along the droplet-substrate interface and increased droplet cooling rates, which rapidly consumed kinetic energy. This finally induced a thicker splat with a smaller spreading diameter. Fig. 7b compares the CFD simulated results with the experimental measurements, showing the experimentally measured flattening ratio is in reasonable agreement with the simulation. This indicated that at the preheating temperature of 300°C, the thermal contact resistance along the splat-substrate interface was in the range of $1 \text{-} 5 \times 10^{-7}$ $m^2 K/W$.

Some analytical models have been developed to understand the droplet spreading process for identifying the key factors influencing the final splat morphologies. The governing equations between these influencing factors and the maximum flattening ratio of splats are briefly summarised in the flowing part. The predicted maximum flattening ratios by these models are compared with our modelling results as well.

Madejski's model [28] was expressed in Eq.16,

$$\frac{3\xi_{m}^{2}}{We} + \frac{1}{Re}(\frac{\xi_{m}}{1.2941})^{5} = 1 \text{ (16)}$$

where ξ_{m} is the maximum flattening ratio. In this model, Madejski only considered the effect of surface tension and viscosity on droplet spreading behaviour. Meanwhile, it assumed that there was no solidification before the maximum spreading and the conditions of $We > 100, Re > 100$.

Zhang's model [29] was expressed in Eq.17,

$$\frac{1}{Re}(\frac{\xi_{m}}{1.18})^{5} + \frac{3(1-\cos\theta)(\xi_{m}^{2}-1)}{We} + S(\frac{\xi_{m}}{1.15})^{2.5} = 1 \text{ (17)}$$

where θ is the contact angle and S=0.005 the solidification parameter. Zhang took into account of the effect of surface tension, viscosity, contact angle and solidification effects by improving Madejski's model. The solution would be more accurate for the condition of $10^4 < Re < 10^6$ and $5 < We < 5 \cdot 10^3$.

Chandra's model [30] was expressed in Eq.18,

$$\xi_m^2 = \frac{We+12}{\frac{3}{8}s^*We+3(1-\cos\theta)+\frac{4We}{\sqrt{Re}}} \quad (18)$$

where $s^* = \dfrac{s}{D_0}$ is the ratio of solidification layer thickness s at the maximum flattening ratio to the particle diameter. This new model was proposed based on the energy conservation of kinetic energy, surface energy, viscous dissipation and solidification. In this model, two parameters i. e. the diameter and thickness of the solidified layer were important in determining the splat diameter.

As shown in Fig. 7b, Madejski's solution overestimated the maximum flattening ratio without the consideration of droplet solidification effects during spreading. Zhang further improved Madejski's model by incorporating solidification process, but this still underestimated the effect of solidification. Chandra's model more accurately predicted the maximum spreading diameters through new approaches analysing the solidification process. It can be seen that the solidification process played an important role in influencing droplet spreading behaviour through consuming a large proportion of inertial energy.

As mentioned above, the increased thermal contact resistance would slow down heat transfer along the droplet-substrate interface. To clearly demonstrate this effect, Fig. 8 depicts the influence of the substrate preheating and thermal contact resistance on temperature evolutions at the droplet top surface and the substrate surface. At the preheating temperature of 150°C, it took more time for the droplet to cool down when the interfacial contact resistance increased from 1×10^{-7} m^{2}K/W to 10×10^{-7} m^{2}K/W as shown in Fig. 8a. In addition, the maximum substrate temperature achieved through droplet heating decreased with the increased thermal contact resistance because it blocked thermal conduction from the droplet to substrate (see Fig. 8b). A similar trend was also noticed on the substrate preheated at 300°C with different thermal contact resistances. Under conditions of the same thermal contact resistance 1×10^{-7} m^{2}K/W, increasing substrate preheating temperature from 27°C to 300°C slowed down the droplet cooling process but increased the maximum temperature of the substrate surface. Importantly, under condition of 300°C preheating temperature with a small thermal contact resistance of 1×10^{-7} m^{2}K/W, the substrate temperature exceeded the melting point. This means that under conditions of good interfacial thermal contact, substrate melting and re-solidification would easily occur. Under these conditions the metallurgical bonding could form between the splat and substrate, potentially improving the interfacial adhesion. In addition, one should note that at the instant the droplet contacts with substrate, the temperature at the substrate surface sharply increases due to fast heat conduction [10].

However the following temperature drop could be related to the formation of air bubbles (as shown in Fig. 3b) which isolated the contact between the droplet and substrate. Once the bubbles detached from the substrate surface, the temperature gradually increased due to further heat conduction.

Figure 9 compares the splat morphologies on substrates preheated at 27°C, 150°C and 300°C with the same thermal contact resistance of 1×10^{-7} m²K/W. Clearly, the droplet almost completed solidification at room temperature indicating a rapid cooling rate, which was also shown in Fig. 8a. The fast growth of the solidification front destabilized the upper liquid flow (see Fig. 3d) and consumed a large fraction of kinetic energy. Therefore only a short finger projected away from the main body which had the smallest contact diameter. At higher preheating temperatures, the solidification process was delayed where a large fraction of liquid was observed. At 150°C the finger projection was supressed and a perfect disk splat was formed accordingly. With preheating temperature increasing to 300°C, the droplet cooling rate was decreased (see Fig. 8a) indicating less consumption of inertial energy. Therefore, more material was still molten and having a high kinetic energy, promoted some liquid jetting away further compared with that at room temperature.

Based on the simulation results, on a substrate with a suitable thermal contact resistance (for example 1×10^{-7} m²K/W), a disk-shaped splat was always formed regardless of the preheating temperature. In reality, some surface adsorbents or moisture adhere onto the substrate which, on heating, will form a thin gas cushion underneath the molten droplet. Thus the interfacial thermal contact resistance would be increased, slowing down the solidification process. Disk-shaped morphologies were observed on substrates even at room temperature when the surface is cleaned by vacuum [31], laser [32] or thermal treatment [33] which evaporate the surface moisture. In addition, the solidification process was an important parameter influencing the splat morphologies. A rapid cooling rate (at room temperature) restricts droplet spreading diameters and induces liquid instabilities to form finger splashing. A relatively slow cooling rate at high substrate temperature reduces the consumption of droplet inertial energy, which ensures some liquid project away from the main body with a high velocity.

3.3 Effect of surface tension

In order to understand the effect of surface tension on droplet spreading, different surface tension values were selected for simulation and the results are shown in Fig. 10. The values of 1.8 n/m ($We = 2355$) and 1.647 n/m ($We = 2574$), represented the surface tension at the melting point and initial droplet temperature respectively. In addition, a small value 1.35 n/m ($We = 3140$) comparable with Ni20Cr material at its melting point, and a temperature-dependent surface tension (see Equation. 19 [34]) were used.

$$\sigma(T) = 1.77 - 3.3\times10^{-4}(T - 1728) \quad 1800\ \text{K} < T < 2100\ \text{K} \quad (19)$$

Figure 10a demonstrates that increased surface tension supressed material projections at the maximum spreading diameter. At the lowest surface tension (the highest We), the high energy liquid material easily jetted away during droplet spreading and induced more material

loss. Therefore the smallest flattening ratio was observed in Fig. 10b while the ratios were similar for the other surface tension values. Generally, the surface tension served as the resistance force in holding the liquid inward during radial flow. At low surface tension, more liquid overcame the surface tension and flowed away from the droplet. When the surface tension increased to 1.647 n/m from 1.35 n/m, material projections were greatly restrained but still generated a short finger at the edge. Once the surface tension increased to 1.8 n/m, a perfect disk splat was formed. Notably, for temperature-dependent surface tension falling in the range of 1.647 n/m and 1.8 n/m, liquid jetting occurred at the maximum spreading diameter. This phenomenon was closely related to the Marangoni convection force due to the surface tension gradient which generated fluid instability inside the droplet [3]. During droplet cooling, the surface tension increased from the top part (high temperature) to the bottom part (low temperature). Thus the Marangoni stress acted from the regions of low surface tension to that of high surface tension and pulled the liquid downwards. Normally the Marangoni number (Ma) was utilized to describe the intensity of Marangoni convection, shown in Eq. 20. The Marangoni convection increases with the Ma number, but can be neglected when Ma is smaller than 80-100 [35].

$$Ma = \frac{\rho C_p D \left| \dfrac{d\sigma}{dT} \right| \Delta T}{2\mu k} \quad (20)$$

where D is the spreading diameter and measured to be 200 μm, ΔT is the temperature distance and measured to be 271 K (when splashing occurred) and $\left| \dfrac{d\sigma}{dT} \right|$ is the surface tension gradient of 3.3×10^{-4} . Therefore the calculated Ma was 124 (larger than 100), indicating severe internal flow around the edge and large velocity fluctuations. The high velocity liquid material would be pushed to strike the protuberant solidified layer, triggering material projects. Two regimes were separated by some researchers to determine whether the capillary force or viscosity dominated the droplet spreading behaviour. Clanet et al. [36] proposed that $\dfrac{We}{Re^{0.8}} > 1$ represented the viscous regime, while Zhang et al. [29] used the criterion of $We > 40.0(1 - \cos\theta)Re^{0.4}$ to stand for the viscous regime. In this paper, the calculated We and Re using the above surface tension values suggested that the viscosity mainly controlled the droplet spreading behaviour. The surface tension alone played little role in changing the splat spreading diameter. However, the surface tension effect cannot be neglected on triggering the formation of liquid jetting and secondary droplets. More splats with splashed fingers were observed for Ni20Cr material as shown in Table 2.

3.4 Effect of contact angle

Figure 11 demonstrates the effect of contact angle on the splat morphologies. Shortly after impact, the droplet spreading diameters increased at a high speed. At this stage, the spreading behaviour was independent of the contact angles because the inertial energy dominated the spreading behaviour. Then the droplet spreading was mainly driven by wetting at the contact

line once the flattening speed of the expanding front slowed. Different splat cross-sectional morphologies were observed due to the contact angle effect [14]. For smaller contact angles (<90°), the capillary force tended to accelerate the contact line during droplet spreading. As the contact angle increased (>90°), the capillary force tended to decelerate the contact line. Once the contact line pinned at the maximum diameter, some upper liquid material would project away if the droplet still possessed enough energy (see Fig. 11a). This was confirmed by Fig. 11b, depicting that a smaller contact angle slightly increased the spreading diameter. Even though the substrate surface wettability (contact angle) played little role in changing the droplet spreading behaviour, it did affect the bubble adhesion on the substrate [37, 38]. With the increased contact angle, the air bubbles tended to remain on the substrate surface, rather than detaching from the surface. This indicated that good wettability was beneficial for bubble detachment.

In fact, the contact angles were closely correlated with the droplet surface tension, and varied with positions along the droplet-substrate interface. Good wetting behaviour enhanced the thermal contact between the droplet and substrate. Accordingly, the interfacial thermal contact resistance would be influenced, which further influenced the droplet spreading behaviour and splat morphologies. As mentioned in section 3.3, low surface tension tended to promote material jetting and slightly reduce the droplet spreading diameter. However, low surface tension would generate the small contact angle, which could facilitate droplet spreading. Thus the reduced droplet spreading diameter resulting from the reduced surface tension would be compensated, or even improved, by the reduced small contact angles. Meanwhile, the good interfacial thermal contact accelerated solidification and arrested droplet jetting. Both factors together contributed to the formation of more disk splats with relatively large spreading diameters, experimentally observed for plasma-sprayed Ni20Cr splats as shown in Table 2.

4 Conclusion

The dynamics of droplet spreading on a stainless steel substrate during plasma spraying was investigated through CFD simulation. The motion of the liquid droplet-air interface and droplet solidification front and bubble formation were precisely captured. Meanwhile, the role of the substrate preheating, interfacial thermal contact resistance, the droplet surface tension and the contact angle on splat morphologies were also studied.

Droplet spreading was mainly driven by the inertial energy before reaching maximum diameter because of the high velocity impinging conditions. Interfacial heat transfer played a key role in influencing droplet spreading behaviour. The solidification process occurred before droplet spreading to the maximum extent on the substrate, even up to a relatively high thermal contact resistance (1×10^{-6} m^{2}K/W in this paper). It would destabilize the upper liquid flow and induce material jetting, depending on the droplet cooling rate. A large thermal contact resistance delayed the droplet solidification process and maintained the droplet in the liquid form. This was beneficial for droplet spreading to a large extent. Under the condition of a thermal contact resistance of 1×10^{-7}-5×10^{-7} m^{2}K/W, the predicted droplet flattening ratios on preheated substrates (150°C or 300°C) agreed well with the experimental results and

Chandra's model. Importantly, splats of disk shape morphology were formed regardless of the substrate preheating temperature when a small thermal contact resistance was developed along the droplet-substrate interface. On the substrate with a high preheating temperature, the substrate surface was easily melted. Larger *We* number resulting from a low surface tension easily provoked material splashing during droplet spreading and generated a relatively smaller flattening ratio under the same condition of small thermal contact resistance (1×10^{-7} m^{2}K/W). The surface tension gradient inside the liquid droplet induced serious material jetting due to the Marangoni convection force. In addition, the droplet spreading behaviour was not very sensitive to the contact angle change under the condition of high cooling rate due to small interfacial thermal contact resistance (1×10^{-7} m^{2}K/W), while a smaller contact angle promoted bubble detachment.

Acknowledgement

References

[1] S. Goutier, M. Vardelle, P. Fauchais, Comparison between metallic and ceramic splats: Influence of viscosity and kinetic energy on the particle flattening, Surf. Coat. Technol., 235 (2013) 657-668.

[2] A. McDonald, M. Lamontagne, C. Moreau, S. Chandra, Impact of plasma-sprayed metal particles on hot and cold glass surfaces, Thin Solid Films, 514 (2006) 212-222.

[3] R. Bhardwaj, J.P. Longtin, D. Attinger, Interfacial temperature measurements, high-speed visualization and finite-element simulations of droplet impact and evaporation on a solid surface, Int. J. Heat Mass Transfer, 53 (2010) 3733-3744.

[4] H. Tabbara, S. Gu, Modelling of impingement phenomena for molten metallic droplets with low to high velocities, Int. J. Heat Mass Transfer, 55 (2012) 2081-2086.

[5] M. Pasandideh-Fard, S. Chandra, J. Mostaghimi, A three-dimensional model of droplet impact and solidification, Int. J. Heat Mass Transfer, 45 (2002) 2229-2242.

[6] A.M. Briones, J.S. Ervin, S.A. Putnam, L.W. Byrd, L. Gschwender, Micrometer-sized water droplet impingement dynamics and evaporation on a flat dry surface, Langmuir, 26 (2010) 13272-13286.

[7] M. Pasandideh-Fard, V. Pershin, S. Chandra, J. Mostaghimi, Splat shapes in a thermal spray coating process: Simulations and experiments, J. Therm. Spray Technol., 11 (2002) 206-217.

[8] Y.Z. Zheng, Q. Li, Z.H. Zheng, J.F. Zhu, P.L. Cao, Modeling the impact, flattening and solidification of a molten droplet on a solid substrate during plasma spraying, Appl. Surf. Sci., 317 (2014) 526-533.

[9] A.T.T. Tran, S. Brossard, M.M. Hyland, B.J. James, P. Munroe, Evidence of substrate melting of nicr particles on stainless steel substrate by experimental observation and simulations, Plasma Chem. Plasma Process., 29 (2009) 475-495.

[10] C. Le Bot, S. Vincent, E. Meillot, F. Sarret, J.-P. Caltagirone, L. Bianchi, Numerical simulation of several impacting ceramic droplets with liquid/solid phase change, Surf. Coat. Technol., 268 (2015) 272-277.

[11] S. Oukach, H. Hamdi, M. El Ganaoui, B. Pateyron, Numerical study of the spreading and solidification of a molten particle impacting onto a rigid substrate under plasma spraying conditions, Thermal Science, 19 (2015) 277-284.

[12] Y.P. Wan, H. Zhang, X.Y. Jiang, S. Sampath, V. Prasad, Role of solidification, substrate temperature and reynolds number on droplet spreading in thermal spray deposition: Measurements and modeling, J. Heat Transfer, 123 (2001) 382-389.

[13] J.B. Lee, D. Derome, R. Guyer, J. Carmeliet, Modelling the maximum spreading of liquid droplets impacting wetting and non-wetting surfaces, Langmuir, 32 (2016) 1299-1308.

[14] K. Yokoi, Numerical studies of droplet splashing on a dry surface: Triggering a splash with the dynamic contact angle, Soft Matter, 7 (2011) 5120-5123.

[15] P. Kritsalis, V. Merlin, L. Coudurier, N. Eustathopoulos, Effect of cr on interfacial interaction and wetting mechanisms in ni alloy/alumina systems, Acta metallurgica et materialia, 40 (1992) 1167-1175.

[16] Y. Zhang, M. Hyland, A.T. Tran, S. Matthews, Effect of substrates temperatures on the spreading behavior of plasma-sprayed ni and ni-20 wt.% cr splats, J. Therm. Spray Technol., 25 (2016) 71-81.

[17] ANSYS FLUENT. 16.0, Theory guide, ANSYS, Inc., 2016.

[18] P.A. Thompson, S.M. Troian, A general boundary condition for liquid flow at solid surfaces, Nature, 389 (1997) 360-362.

[19] K. Yokoi, D. Vadillo, J. Hinch, I. Hutchings, Numerical studies of the influence of the dynamic contact angle on a droplet impacting on a dry surface, Phys. Fluids, 21 (2009) 072102.

[20] M. Renardy, Y. Renardy, J. Li, Numerical simulation of moving contact line problems using a volume-of-fluid method, J. Comput. Phys., 171 (2001) 243-263.

[21] S.F. Lunkad, V.V. Buwa, K.D.P. Nigam, Numerical simulations of drop impact and spreading on horizontal and inclined surfaces, Chem. Eng. Sci., 62 (2007) 7214-7224.

[22] H. Kobatake, J. Brillo, Density and viscosity of ternary cr–fe–ni liquid alloys, J. Mater. Sci., 48 (2013) 6818-6824.

[23] S. Mukherjee, W.L. Johnson, W.K. Rhim, Noncontact measurement of high-temperature surface tension and viscosity of bulk metallic glass-forming alloys using the drop oscillation technique, Appl. Phys. Lett., 86 (2005) 014104.

[24] M. Xue, Y. Heichal, S. Chandra, J. Mostaghimi, Modeling the impact of a molten metal droplet on a solid surface using variable interfacial thermal contact resistance, J. Mater. Sci., 42 (2007) 9-18.

[25] A. McDonald, C. Moreau, S. Chandra, Effect of substrate oxidation on spreading of plasma-sprayed nickel on stainless steel, Surf. Coat. Technol., 202 (2007) 23-33.

[26] J.U. Brackbill, D.B. Kothe, C. Zemach, A continuum method for modeling surface tension, J. Comput. Phys., 100 (1992) 335-354.

[27] M. Qu, A. Gouldstone, On the role of bubbles in metallic splat nanopores and adhesion, J. Therm. Spray Technol., 17 (2008) 486-494.

[28] J. Madejski, Solidification of droplets on a cold surface, Int. J. Heat Mass Transfer, 19 (1976) 1009-1013.

[29] H. Zhang, Theoretical analysis of spreading and solidification of molten droplet during thermal spray deposition, Int. J. Heat Mass Transfer, 42 (1999) 2499-2508.

[30] R. Dhiman, S. Chandra, Freezing-induced splashing during impact of molten metal droplets with high weber numbers, Int. J. Heat Mass Transfer, 48 (2005) 5625-5638.

[31] X. Jiang, Y. Wan, H. Herman, S. Sampath, Role of condensates and adsorbates on substrate surface on fragmentation of impinging molten droplets during thermal spray, Thin Solid Films, 385 (2001) 132-141.

[32] H. Li, S. Costil, H.L. Liao, C.J. Li, M. Planche, C. Coddet, Effects of surface conditions on the flattening behavior of plasma sprayed cu splats, Surf. Coat. Technol., 200 (2006) 5435-5446.

[33] M. Fukumoto, H. Nagai, T. Yasui, Influence of surface character change of substrate due to heating on flattening behavior of thermal sprayed particles, J. Therm. Spray Technol., 15 (2006) 759-764.

[34] J. Brillo, I. Egry, Surface tension of nickel, copper, iron and their binary alloys, J. Mater. Sci., 40 (2005) 2213-2216.

[35] G. Lu, Y.-Y. Duan, X.-D. Wang, D.-J. Lee, Internal flow in evaporating droplet on heated solid surface, Int. J. Heat Mass Transfer, 54 (2011) 4437-4447.

[36] C. Clanet, C. Béguin, D. Richard, D. Quéré, Maximal deformation of an impacting drop, J. Fluid Mech., 517 (2004) 199-208.

[37] V. Mehdi-Nejad, J. Mostaghimi, S. Chandra, Air bubble entrapment under an impacting droplet, Phys. Fluids, 15 (2003) 173-183.

[38] J. San Lee, B.M. Weon, J.H. Je, K. Fezzaa, How does an air film evolve into a bubble during drop impact?, Phys. Rev. Lett., 109 (2012) 204501.

Figure captions

Fig. 1. Computational geometry and boundary conditions for simulation of droplet spreading.

Fig. 2. Characterisation of droplet flattening ratios using different grid spacing.

Fig. 3. Droplet spreading, solidification and flow streamlines with time elapse are shown in (a) while (b) represents the magnified view of areas marked in (a).

Fig. 4. 3D simulation results of splat morphologies, (a) top view and (b) cross section.

Fig. 5. Typical splat morphologies of disk shapes, (a) disk shape with short fingers and (b) perfect disk shape.

Fig. 6. The evolution of droplet spreading diameter as a function of the thermal contact resistance at the substrate preheating temperature of 150°C, (a) splat morphology at the maximum spreading diameter, (b) droplet flattening ratios with comparison of experiments.

Fig. 7. The evolution of droplet spreading diameter as a function of the thermal contact resistance at the substrate preheating temperature of 300°C with a contact angle of 60°, (a) splat morphology at the maximum spreading diameter, (b) droplet flattening ratios with comparison of theoretical models and experiments.

Fig. 8. Temperature evolution of (a) the droplet surface and (b) substrate surface under different conditions of substrate preheating temperature and thermal contact resistance.

Fig. 9. Comparison of the splat morphology at the maximum spreading diameter on substrates preheated at different temperatures with thermal contact resistance of 1×10^{-7} m^2K/W.

Fig. 10. The evolution of droplet spreading diameter as a function of the surface tension at the substrate preheating temperature of 300°C, (a) splat morphology at the maximum spreading diameter, (b) droplet flattening ratios.
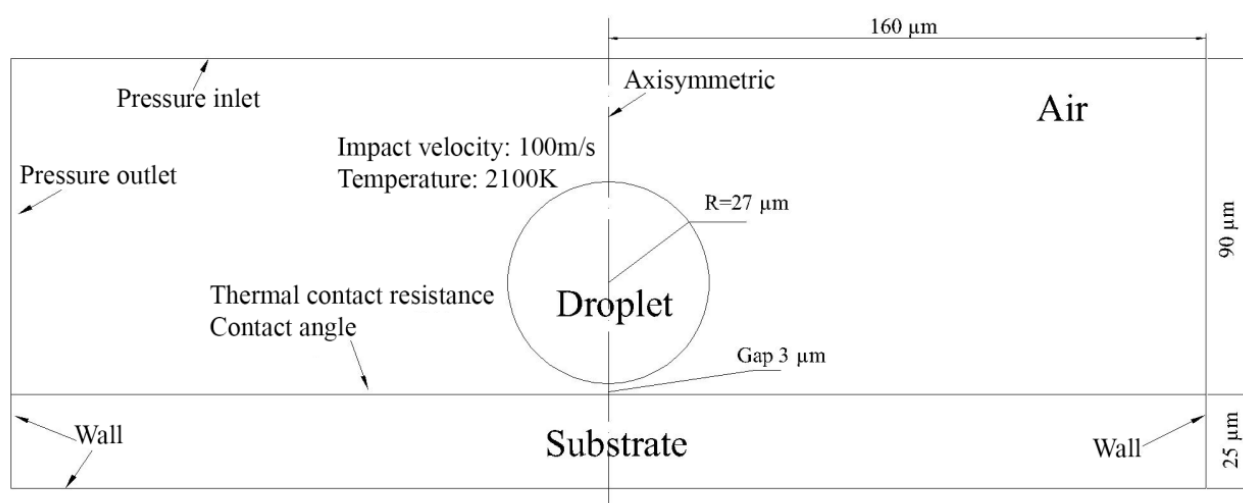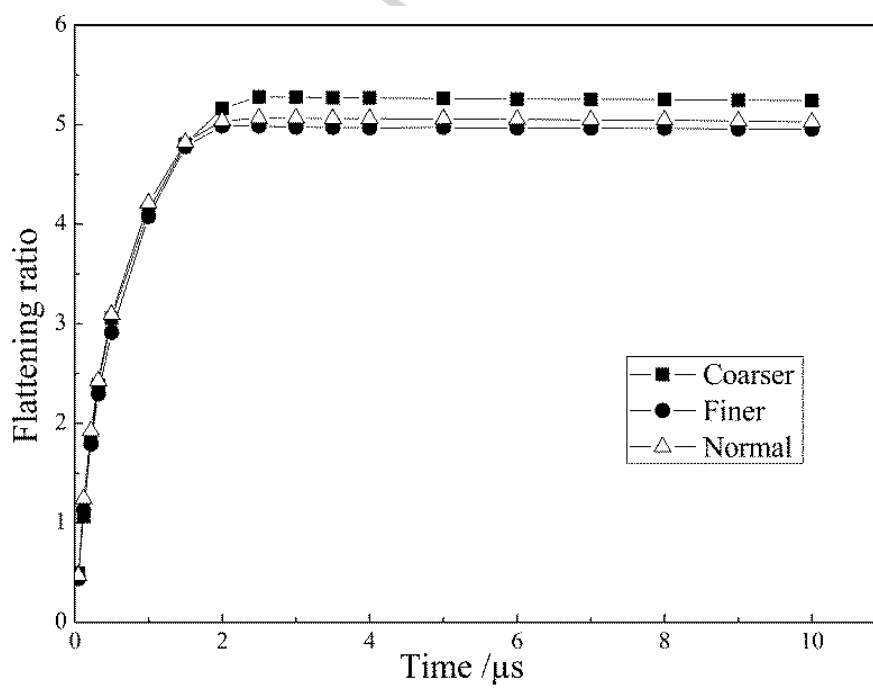
Fig. 11. The evolution of droplet spreading diameter as a function of the contact angle at the substrate preheating temperature of 300°C, (a) splat morphology at the maximum spreading diameter, (b) droplet flattening ratios.
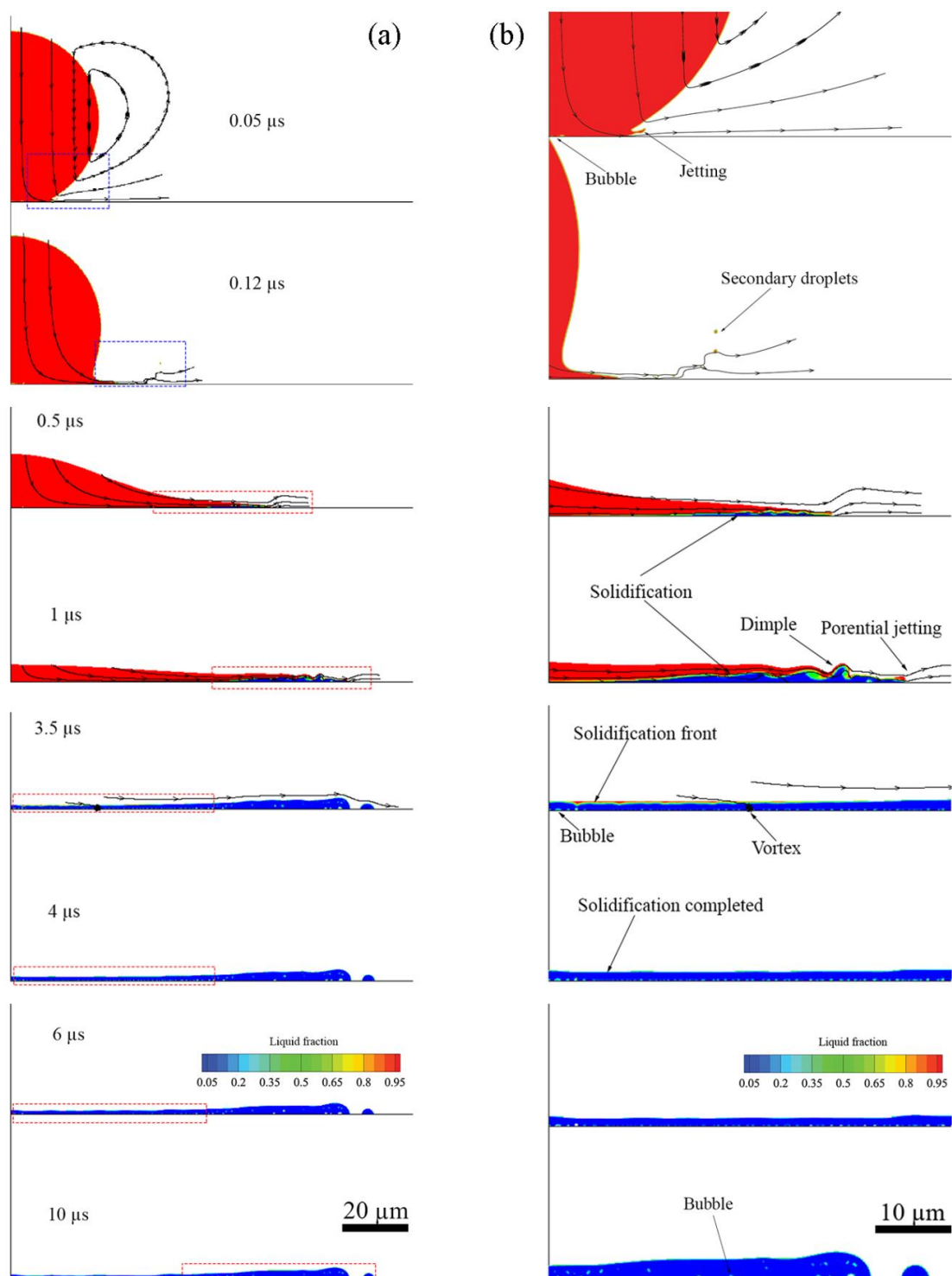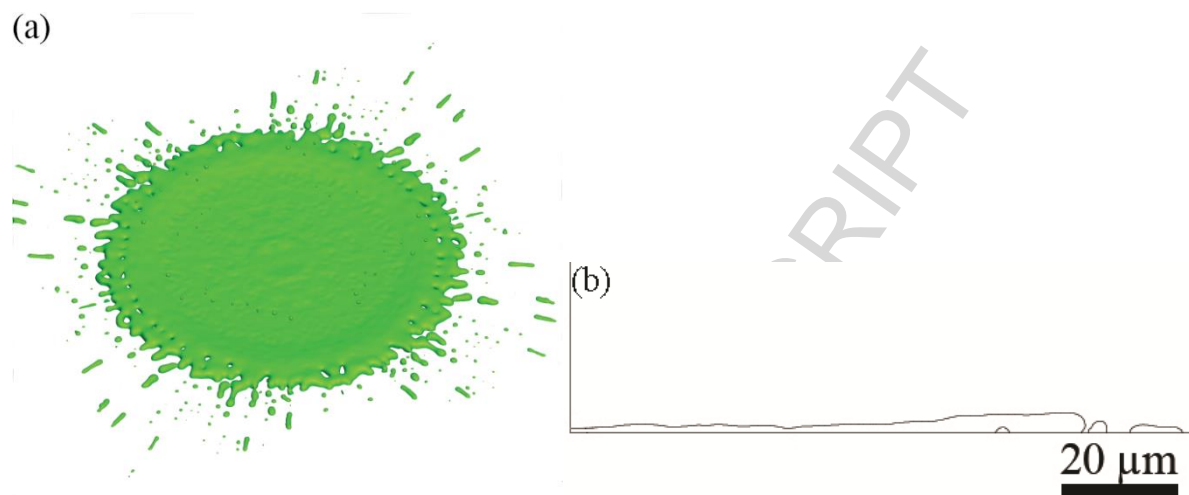
Fig. 1.

Fig. 2.

Fig. 3.

(a)

(b)

Fig. 4.

(a)
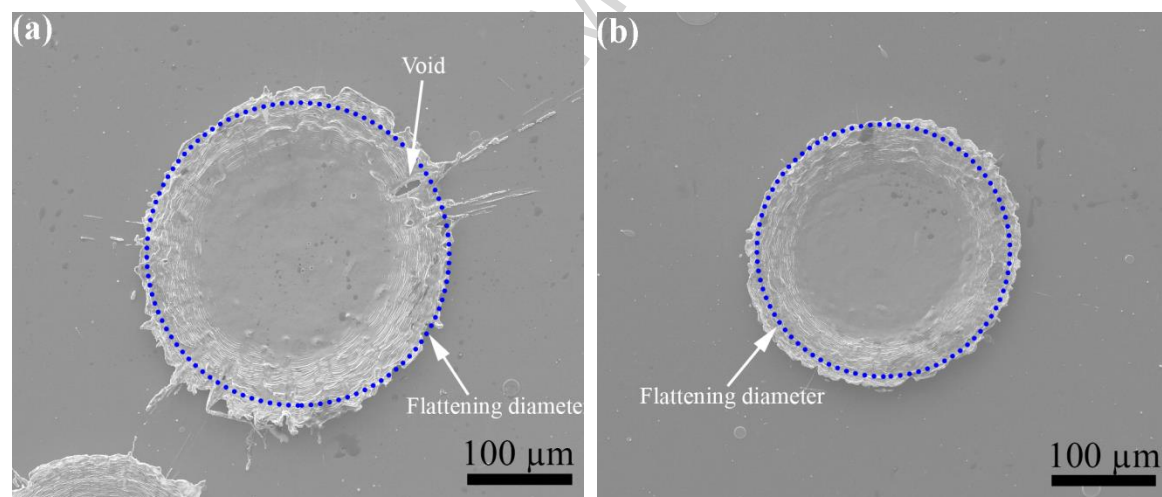

(b)

20 μm

Fig. 5.

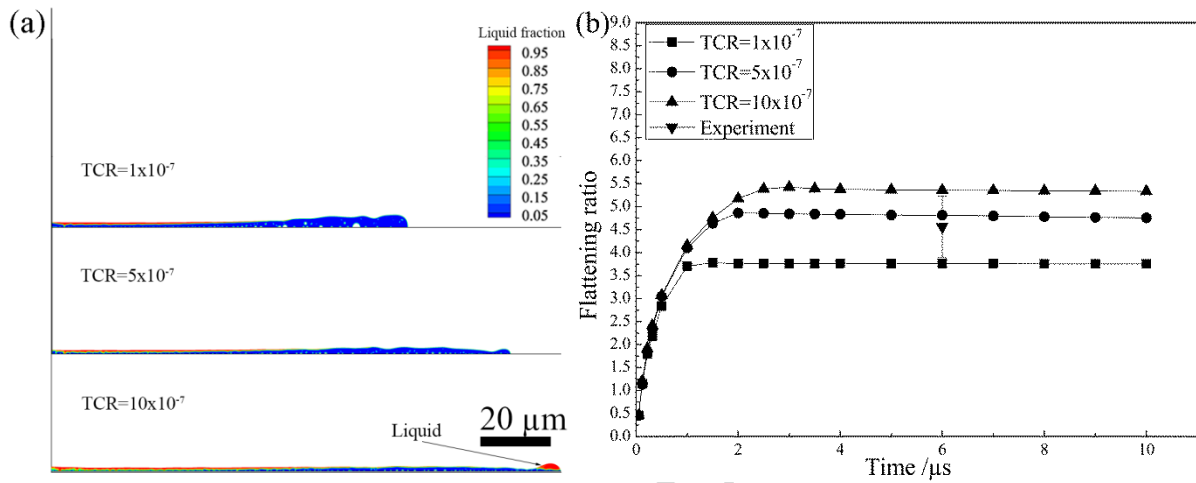(a) Void

Flattening diameter

100 μm

(b) Flattening diameter

100 μm

Fig. 6.

Fig. 7.

Fig. 8.

Fig. 9.

Fig. 10.

Fig. 11.

(a) Contact angle 60°, Contact angle 90°, Contact angle 120°, Liquid fraction, 20 µm
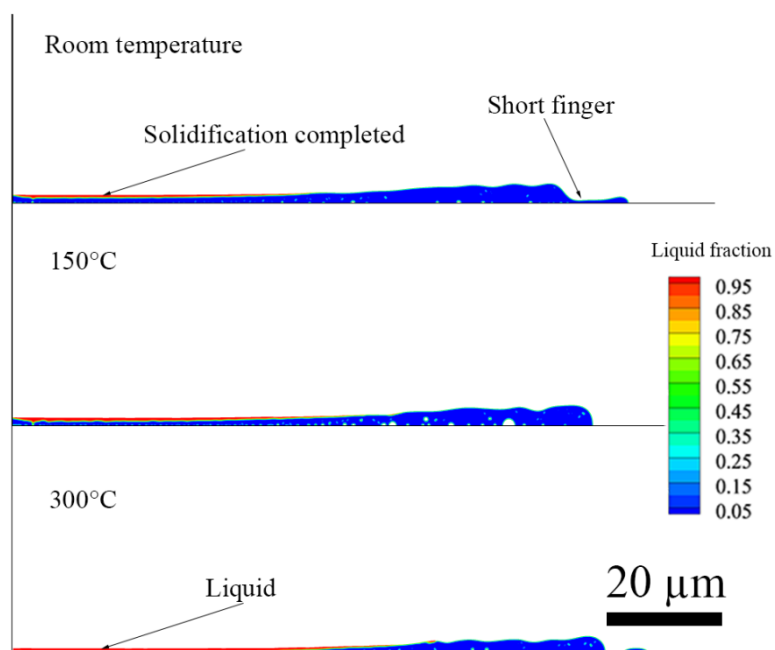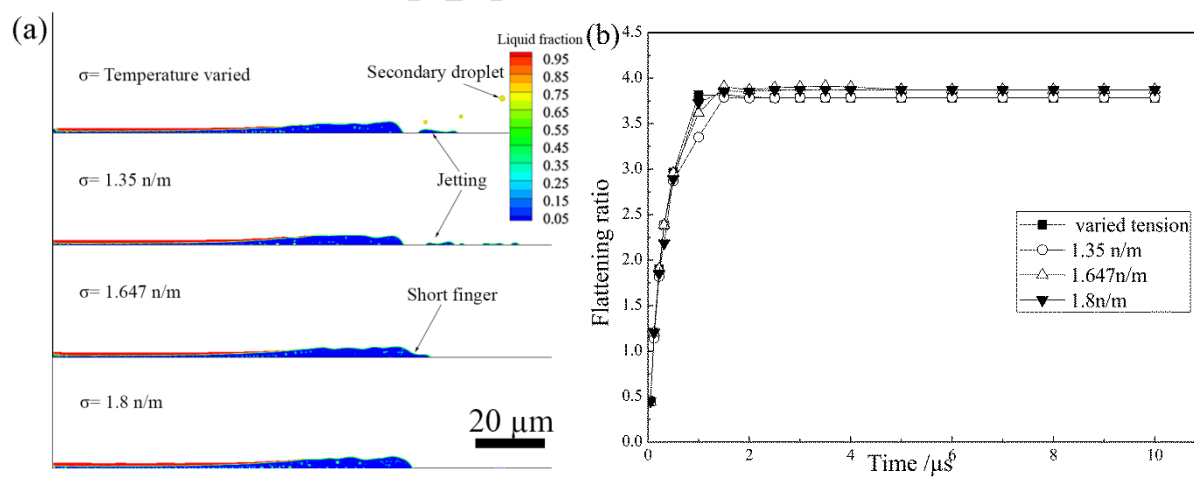
(b) Flattening ratio vs Time /µs, 60°, 90°, 120°
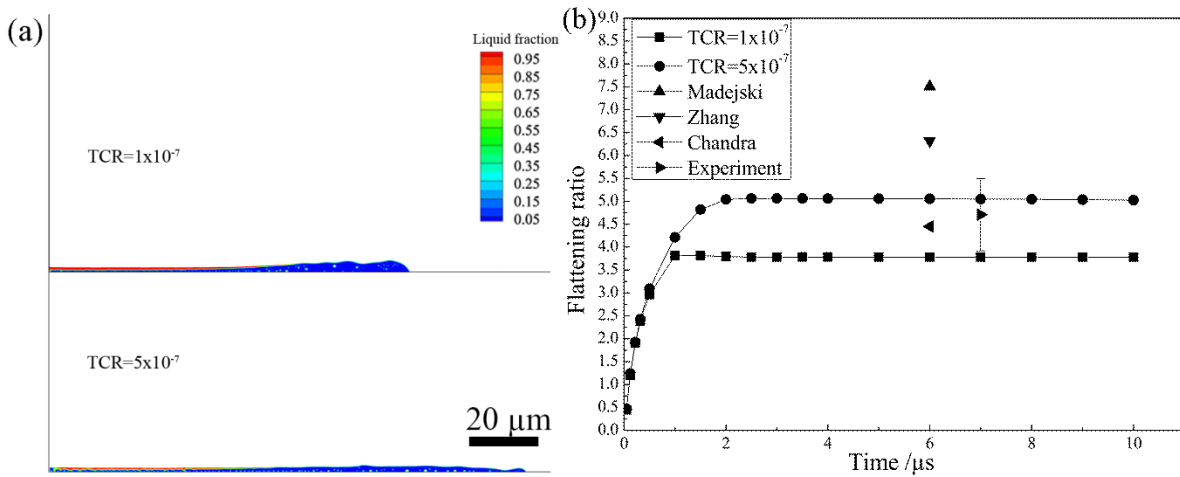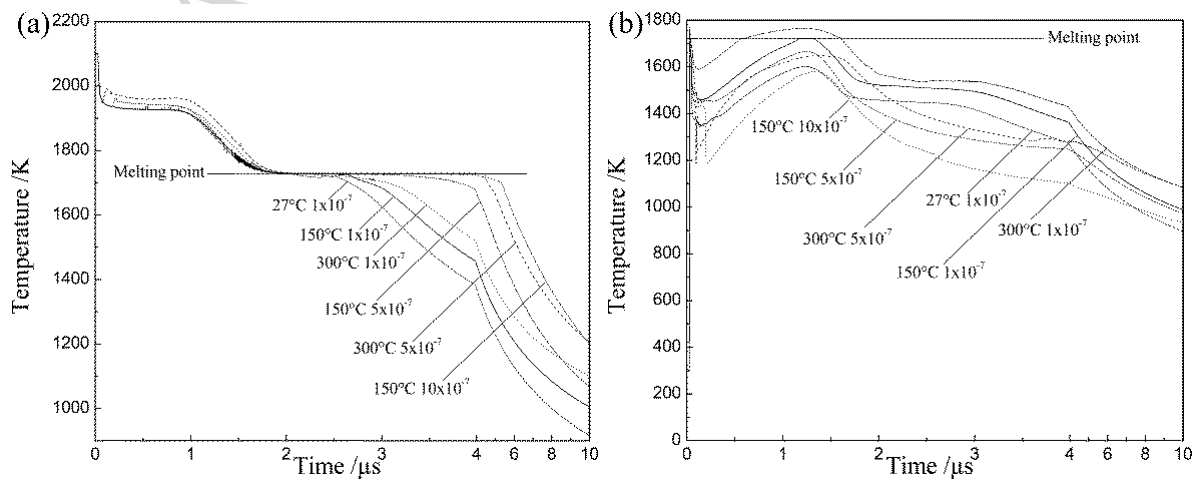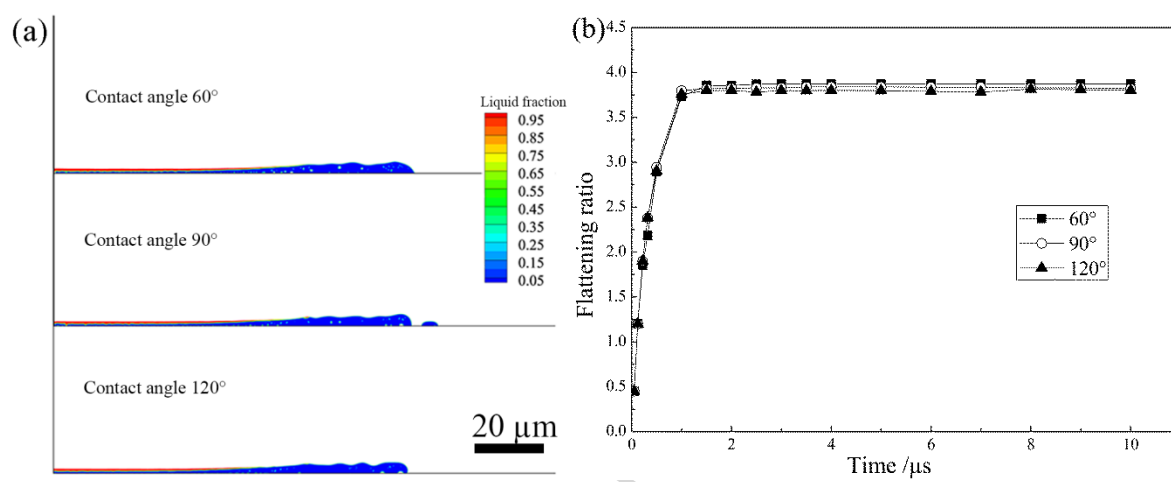
Highlights

- Droplet spreading behaviour in the plasma spraying process is numerically studied.
- Modelling results are compared to experimental observation of Ni and Ni20Cr splats.
- Interfacial heat transfer is the key factor influencing droplet spreading dynamics.
- Higher *We* induced by surface tension changes promotes liquid jetting.
- Droplet contact angles play an insignificant role in influencing splat diameters.